The Influence of Tropical Forcing on Extreme Winter Precipitation in the Western Himalaya

Forest Cannon[1,2], Leila M.V. Carvalho[1,2], Charles Jones[1,2], Andrew Hoell[3],

Jesse Norris[2], George N. Kiladis[3], Adnan A. Tahir[4]

[1] Department of Geography, University of California, Santa Barbara, USA

[2] Earth Research Institute, University of California, Santa Barbara, USA

[3] NOAA Earth System Research Laboratory, Physical Sciences Division, Boulder, Colorado, USA

[4] Department of Environmental Science, COMSATS Institute of Information Technology, Pakistan

Corresponding author address:

Forest Cannon

Department of Geography, University of California, Santa Barbara

Santa Barbara, CA 93106, USA

Email: fcannon@geog.ucsb.edu

Abstract

Within the Karakoram and western Himalaya (KH), snowfall from Winter Westerly Disturbances (WD) maintains the region's snowpack and glaciers, which melt seasonally to sustain water resources for downstream populations. WD activity and subsequent precipitation are influenced by global atmospheric variability and tropical-extratropical interactions. On interannual time-scales, El Niño related changes in tropical diabatic heating induce a Rossby wave response over southwest Asia that is linked with enhanced dynamical forcing of WD and available moisture. Consequently, extreme orographic precipitation events are more frequent during El Niño than La Niña or neutral conditions. A similar spatial pattern of tropical diabatic heating is produced by the MJO at intraseasonal scales. In comparison to El Niño, the Rossby wave response to MJO activity is less spatially uniform over southwest Asia and varies on shorter time-scales. This study finds that the MJO's relationship with WD and KH precipitation is more complex than that of ENSO. Phases of the MJO propagation cycle that favor the dynamical enhancement of WD simultaneously suppress available moisture over southwest Asia, and vice versa. As a result, extreme precipitation events in the KH occur with similar frequency in most phases of the MJO, however, there is a transition in the relative importance of dynamical forcing and moisture in WD to orographic precipitation in the KH as the MJO evolves. These findings give insight into the dynamics and predictability of extreme precipitation events in the KH through their relationship with global atmospheric variability, and are an important consideration in evaluating Asia's water resources.

1. Introduction

Extratropical cyclones that affect southwest Asia from November through April are the primary climatic influence in the Karakoram and western Himalaya (KH) during non-monsoon months (Singh et al. 1995; Lang and Barros, 2004; Barlow et al. 2005; Dimri et al. 2015). In excess of 50% of the total annual precipitation in the KH is delivered by fewer than ten of these " winter westerly disturbance" (WD) events each winter season (Lang and Barros, 2004; Barlow et al. 2005; Barros et al. 2006; Bookhagen and Burbank, 2010; Cannon et al. 2014). Their associated frontal systems interact with topography to produce heavy orographic precipitation, while the lapse-rate ensures that precipitation falls as snow over the KH's high mountains. Snowfall generated by WD maintains regional snowpack and glaciers (Anders et al. 2006; Tahir et al. 2011; Bolch et al. 2012; Ridley et al. 2013; Cannon et al. 2015), and is essential to water resources for downstream populations (Immerzeel et al. 2009; Bolch et al. 2012; Hewitt, 2014).

Significant relationships exist between WD activity over southwest Asia (25-40°N; 40-80°E) and global modes of climate variability, including; the Madden-Julian Oscillation (MJO) (Barlow et al. 2005; Hoell et al. 2012), the El Niño Southern Oscillation (ENSO) (Syed et al. 2006; Yadav et al. 2010; Hoell et al. 2013), the Arctic Oscillation/North Atlantic Oscillation (NAO) (Gong et al. 2001; Wu and Wang, 2002, Yadav et al. 2009; Syed et al. 2010; Filippi et al. 2014) and the Polar Eurasia Pattern (Lang and Barros, 2004). During the boreal winter, southwest Asia, and specifically the Karakoram, are within the subtropical belt of upper-level westerlies (Krishnamurti, 1961), which serve as a baroclinic wave-guide (Wallace et al. 1988). Variability in the upper-level jet over southwest Asia, and subsequent variability in shear, maximum wind speed, and deformation, has a complex relationship with WD activity (Barlow et al. 2005). Large-scale changes in atmospheric circulation that modify the jet, such as ENSO (Rasmussen and Carpenter, 1982; 1983), the NAO (Barnston and Livezey, 1987) and the MJO (Madden and Julian, 1972; 1994), significantly modify the frequency and intensity of WD, thereby altering seasonal precipitation totals in High Asia (Yadav et al. 2009; Dimri et al. 2012; Fillippi et al. 2014). Furthermore, these modes influence low-level circulation and moisture conditions, resulting in important differences in the background atmosphere with which individual WD interact. It appears that the influence of global modes of variability on KH precipitation is more complex than previously appreciated, as both upper-level dynamics and thermodynamic conditions over southwest Asia can be modified uniquely, thus altering the development of

WD and orographic precipitation in a manner that is not well-documented in the literature addressing this region's climate to date (Cannon et al. 2015).

Previous studies have typically explored how precipitation in the KH is related to global modes of climate variability at monthly or seasonal scales (e.g. Archer and Fowler, 2004; Lang and Barros, 2004; Dimri, 2012; Fillippi et al. 2014; Cannon et al. 2014). WD exist at synoptic-scales, between 2 and 7 days, therefore it is important to investigate these relationships using daily data with a specific focus on extreme events, which numerous studies attempting to quantify regional precipitation have found to contribute the vast majority of seasonal precipitation (Hewitt, 2005; Fillippi et al. 2014; Cannon et al. 2014, 2015). Cannon et al. (2015) investigated individual WD events and demonstrated significant event-to-event differences in the contribution of upper-level circulation and low-level moisture to extreme precipitation in the KH over the period 1979-2013. This work found that seasonal changes in the atmosphere regulated the relative importance of dynamic and thermodynamic components of WD systems to orographic precipitation generation, suggesting that intraseasonal and interannual variability, which also produce large-scale changes in circulation and moisture availability, may be an additionally important consideration for understanding regional precipitation. In the current manuscript we explore the role of ENSO and the MJO in modifying WD and subsequent KH precipitation through tropical forcing.

Heat, moisture and momentum exchanges relate intraseasonal and interannual variability in the atmosphere to severe weather and extreme precipitation in the extratropics, and are fundamental to understanding how the MJO and ENSO influence storm tracks (Lee and Lim, 2012; Takahashi and Shirooka, 2014), including WD. The basis of the linkage between the tropics and southwest Asia is in a forced Rossby wave response of the upper troposphere to stationary diabatic heating anomalies in the tropics (Barlow et al. 2005), which resembles a Gill-Matsuno-like response (Matsuno 1966; Gill 1980). During enhanced convection over the eastern Indian Ocean, local upper-level divergence intensifies and forces anomalous subsidence over southwest Asia. Both ENSO and the MJO produce similar spatial patterns of anomalous diabatic heating in the tropics, but the considerable differences in time-scales and Rossby wave responses over southwest Asia produce differing relationships with the region's climate.

On interannual time-scales, the Rossby wave response to El Niño increases southwest Asia precipitation by weakening climatological subsidence over the region (Hoell et al. 2013). A Rossby wave response is also generated by the MJO on intraseasonal scales, and is responsible for increased precipitation over southwest Asia as a result of anomalous regional ascent (Barlow et al. 2005). However, in comparison to El Niño, the Rossby wave response to MJO activity is less spatially uniform over southwest Asia and exists on a much shorter time-scale. Consequently, this mode's relationship with WD and KH precipitation is more complex. Although the KH is within the larger southwest Asia domain and similarly relies on WD to deliver precipitation, we will illustrate that the response to tropical forcing at intraseasonal scales is unique relative to previous results that investigated southwest Asia as a whole (e.g. Barlow et al. 2005; Hoell et al. 2012), largely on account of the KH's extreme topography and location. Here, we perform a comprehensive study of the role of tropical forcing on winter storms in the KH.

This manuscript discusses the frequency of extreme precipitation events in the KH during different phases of ENSO and the MJO, and individual mechanisms within WD events that relate large-scale tropical forcing by the MJO and ENSO to extreme orographic precipitation in the KH. Understanding the dynamics behind the independent and combined influences of the MJO and ENSO on WD variability and extreme precipitation in the KH is essential to understanding the region's hydrology. These weather-climate relationships will lead to better forecasting of winter storms (Schubert et al. 2002; Barlow et al. 2005) and long-term predictability of water resources over southwest Asia and the KH (Immerzeel et al. 2009; Ridley et al. 2013).

2. Data

a. Precipitation Datasets

Meteorological data from the sparse network of stations within topographically complex High Asia is limited. Furthermore, extant data can be of marginal quality due to sampling errors or biases (Anders et al. 2006; Bookhagen and Burbank, 2010; Maussion et al. 2014). In this research, the influence of ENSO and the MJO on large-scale winter (November to April) precipitation over High Asia and surrounding regions is investigated using satellite observations from the Tropical Rainfall Measurement Mission 3B42V7 (TRMM), interpolated station data from the Asian Precipitation Highly Resolved Observational Data Integration Towards Evaluation (APHRODITE) dataset, and reanalysis precipitation from Climate Forecast System Reanalysis (CFSR). Precipitation in the KH is additionally investigated using a set of meteorological stations maintained by the Pakistani Meteorological Department and the Water and Power Development Authority of Pakistan.

TRMM 3B42V7 is a multi-satellite data set that provides near-global 0.25° resolution precipitation estimates at three-hour intervals for the period 1998-2015 (Huffman 2007). TRMM has well known deficiencies in estimating light precipitation as well as solid-state precipitation (Barros et al. 2000, 2006; TRMM Working Group Summaries). APHRODITE (Yatagai et al. 2009) is produced using distance-weighted interpolation between station observations, and is available at daily 0.25° resolution over Asia for the period 1951-2007. This product is included as an additional measure of robustness, but performs less than ideally over High Asia, where observations are sparse and topography is complex (Anders et al. 2006; Bookhagen and Burbank, 2006). CFSR precipitation, at 0.5° horizontal resolution, is too coarse to resolve the complexities of orographic precipitation in the KH, but along with TRMM and APHRODITE is used to evaluate the timing of extreme events. Cannon et al. (2014, 2015) have utilized these precipitation datasets for similar studies and further documented their efficacy in the study region. Additionally, Norris et al. (2015a,b) have evaluated TRMM precipitation in comparison to dynamically downscaled precipitation using the Weather Research and Forecasting model (Skamarock et al. 2008) over the study region and found their general distributions to be correlated significantly, though as Norris et al. (2015a) exhibit, there is less consistency amongst precipitation products at high elevations.

Data from 12 in-situ stations spread over northern Pakistan at altitudes between 1,260 and 4,440m are also employed in this study (similar to Palazzi et al. 2015). The principal characteristics of the stations—altitude, coordinates, temporal resolution and managing agency—are detailed in Table 1, and their locations, along with a reference map of the study region, are shown in Fig. 1. Here, we consider daily-accumulated precipitation from seven PMD stations for the period 1960-2012. Additionally, we utilize 15 years (1995-2009) of daily-accumulated precipitation from five meteorological stations in the ablation zone of the Upper Indus Basin that are maintained by the Water and Power Development Authority of Pakistan (WAPDA). WAPDA stations are used for validation of the longer PMD record during overlapping periods, and indicate good agreement amongst the timing of extreme events (not shown here). Here, we assume that extant biases in the magnitude of station-measured precipitation in the KH

(Hewitt et al. 2014) are constant in time and thus do not affect the selection of extreme events relative to all other dates in the record.

b. Meteorological Data from Reanalyses

CFSR data, from the National Centers for Environmental Prediction (Saha et al. 2010), are used to investigate large-scale climate and the dynamics of WD. CFSR is available at 0.5° horizontal-resolution for the period 1979-2013. CFSR was chosen on account of its model coupling, spatial resolution, and modern data assimilation system (Saha et al. 2010). Analysis of geopotential height, omega, wind, moisture, and temperature are performed at near-surface, 850, 500 and 200-hPa levels with daily temporal resolution. Anomaly fields were derived by removing the mean seasonal cycle over the duration of the timeseries.

c. Outgoing Longwave Radiation

This study uses National Oceanic and Atmospheric Administration – Daily Climate Data Record PSD Interpolated Version outgoing longwave radiation (OLR) data (1° resolution), consisting of satellite observed mean OLR at the top of the atmosphere (Lee, 2014).

d. Intraseasonal and Interannual Indices

MJO events are identified using the methodology of Jones (2009), in which combined empirical orthogonal function (EOF) analysis of equatorially averaged (15°S-15°N) 20-200 day bandpass-filtered anomalies of outgoing longwave radiation, 200-hPa zonal wind and 850-hPa zonal wind yields first and second EOFs that are in good agreement with those of Wheeler and Hendon (2004). The phase diagram of the first two normalized principal components approximately follows the eight-phase convention of the real-time multivariate MJO index of Wheeler and Hendon (2004). The primary difference between this approach and that of Wheeler and Hendon (2004) is the use of bandpass filtered anomalies, which more accurately represent the temporal evolution of MJO events. In this study, an MJO event was defined when 1) the phase angle between the first two principal components systematically rotated anticlockwise, indicating eastward propagation at least to phase 5; 2) the amplitude was always larger than 0.35; 3) the mean amplitude during the event was larger than 0.9; and 4) the entire duration of the event lasted between

30 and 90 days. Based on these conditions, all MJO events identified in this study started in phases 1–4, propagated eastward, and ended in phases 4–8 (i.e., isolated events) or restarted from previous MJO occurrences (i.e., successive events; phase continues from 8 to 1). Further details can be found in Jones (2009).

It is important to consider that the use of different MJO indices may lead to disparate conclusions concerning MJO timing and strength (Kiladis et al. 2014). Thus, the analyses presented in this study were additionally performed using the real-time multivariate MJO index of Wheeler and Hendon (2004), which is also circulation based, as well as an OLR-only version of the Jones (2009) index and the OLR MJO Index (OMI, Kiladis et al. 2014). Although the general features of circulation and OLR for MJO composites (discussed in section 4) are similar regardless of index, diversity in the amplitude and phase of individual MJO events according to the index used does produce moderately dissimilar distributions of extreme KH precipitation events across the eight phases of the MJO (section 3). Despite the sensitivity of event distributions to the choice of MJO index on account of the relatively small number of total extreme events (< 10 per phase of the MJO in ENSO neutral conditions), the composites of circulation and moisture during these events (section 5) are extremely similar across indices, as the majority of dates considered for the composites do not change. Furthermore, dates that do not correspond between indices still exhibit similar OLR anomalies in the tropics (the temporal evolution of the various MJO indices are similar), and their effect on large-scale circulation remains consistent. Consequently, the discussion of the mechanisms that link KH precipitation to MJO variability presented here is not especially sensitive to the choice of MJO index. The Jones (2009) index was ultimately selected for this study based on the advantage of filtering out day-to-day variability that is included in the real-time multivariate MJO index, as well as the inclusion of large-scale circulation, which is not considered in OLR-only indices.

ENSO variability was defined based on the Oceanic Niño index, which is calculated by averaging sea surface temperature for the Niño 3.4 region and applying a 3-month running mean (Trenberth, 1997). Data were retrieved from the National Oceanic and Atmospheric Administration's Climate Prediction Center website. ENSO conditions were classified based on monthly ONI values greater than 0.5 (El Niño), less than -0.5 (La Niña), and between -0.5 and 0.5 (neutral).

3. Extreme Precipitation Events

a. Extreme Precipitation Event Definition

Throughout this manuscript, analyses of individual events are performed based on the identification of extreme precipitation using a combination of CFSR and PMD station data. Principal component analysis of the PMD station data for Nov.-Apr. was performed using a covariance matrix to reduce the number of variables by identifying a leading orthogonal pattern of variability that represents heavy precipitation dates at all seven stations from 1960 to 2012 (Wilks, 2006). The first principal component explained 53% of the variability amongst stations, and high values were observed to correspond to high-magnitude precipitation at multiple PMD stations, with heavy precipitation that was widely distributed over the KH in CFSR. Independent 90th percentile dates (only the highest magnitude day of all consecutive 90th percentile days is retained) from the station-based first principal component timeseries and independent 90th percentile dates from aggregated CFSR precipitation in the KH (73-78°E, 34-37°N) produced a collection of extreme precipitation events that overlapped or occurred within a 1-day lag period in 205 cases, or approximately 67% of the time, (PMD had 295 independent events and CFSR had 308) during Nov.-Apr., 1979-2012. These 205 overlapping extreme events are used throughout the manuscript to investigate how tropical forcing relates to WD and KH precipitation during the few days that account for the majority of regional precipitation. The approximately 33% of events that did not correspond between datasets were generally associated with precipitation totals slightly below the extreme event threshold in both datasets or above the threshold for only one of the datasets. These events were discarded from further evaluation. However, analyses that did include these events were not inconsistent with the results presented here.

b. Contribution of Extreme Events to Seasonal and Annual Precipitation

Table 2 shows the distribution of precipitation at individual stations, their relationship with the first principal component that represents the combined variance of all stations, and the percent contribution of the 205 identified extreme events to total precipitation. Total precipitation for 3-day periods centered on the 205 events, which accounts for less than 10% of all winter days, comprised 67% of total PMD averaged precipitation for Nov.-Apr., 1979-2012 and 36% of precipitation for all dates from 1979-2012. The 205 winter events contributed between 52 and 76% of total winter precipitation and between 30 and 43% of total annual precipitation at individual PMD stations over the 34-year study period. The considerable contributions to annual precipitation exhibited here are likely too low, as the magnitude of precipitation in winter is severely underestimated on account of difficulties in measuring snowfall in the KH (Palazzi et al. 2015; Norris et al. 2015b). Additionally, each individual station's precipitation correlates significantly (greater than 0.7) to the first principal component that represents their combined variability, and alpha values below 1.0 indicate gamma distributions that are skewed to the right (Wilks, 2006) and are representative of infrequent moderate-heavy precipitation, which accounts for a comparatively large amount of the seasonal total (Jones et al. 2004). With respect to average annual precipitation reported in Table 2, it is important to note that these stations are located in valleys, which receive three to five times less precipitation than is observed on surrounding mountains during winter storms (Hewitt, 2005; 2014). The precipitation statistics reported here illustrate the importance of the extreme events investigated throughout this manuscript to KH climate and regional water resources.

c. Intraseasonal and Interannual Variability in the Distribution of Events

The differences in the number of events according to MJO and ENSO conditions are presented here as motivation to better understand the relationships between tropical forcing, WD and KH precipitation. The number of extreme precipitation events in the KH per winter season is shown in Fig. 2, which additionally identifies seasons with predominantly El Niño, Neutral or La Niña conditions. A significant long-term trend in the number of events per season is not readily identified, though the most noticeable feature in the timeseries is the near decade-long period of below average values immediately following the 1997-98 El Niño. This period included three weak El Niño seasons and four La Niña seasons. Though ENSO is not the only influence on extreme events, the Niño 3.4 index is significantly correlated ($p < 0.05$ via a Monte Carlo Simulation) to the number of extreme events per season, with a Pearson moment correlation of 0.41 (removing the 1997/98 El Nino reduces this correlation to 0.31, which is still significant, but highlights that a few strongly correlated seasons contribute considerably to the relationship). The average number of extreme events per season during El Niño conditions (9 seasons) is 6.8, while during La

Niña conditions (9 seasons), this value drops significantly (t-test; $p<0.05$) to 5.4. The number of events in Neutral conditions (15 seasons) averages to 5.9. Additionally, the maximum number of events observed in a single year (10) was recorded during the 1997-98 El Niño, while the minimum number (2) was recorded during the 2000-01 La Niña.

Figure 3 displays the percentage of days within each phase of MJO activity that recorded an extreme precipitation event in the KH during winter seasons, 1979-2012. These statistics are additionally categorized according to ENSO conditions. We note that the distribution of events across phases is somewhat sensitive to the choice of MJO index, but that the overall conclusions presented here are consistent across the four indices tested (see Section 2). According to the Jones (2009) MJO index, phases 6, 7 and 8, experience proportionally more events than non-active MJO conditions, indicated here as phase 0. The frequency of events in MJO phases 1-4 are close to the proportions of non-active MJO, while the only phase that produces appreciably fewer extreme events is phase 5. The differences between the number of events per phase are not statistically significant. The relatively consistent distribution of extreme precipitation events in the KH across phases is interesting given that previous research has defined significant relationships between phases of the MJO and stormtracks (Lee and Lim, 2012; Penny et al. 2012) and has also found precipitation over southwest Asia as a whole to vary according to MJO phase (Barlow et al. 2005; Hoell et al. 2014). Spatial differences in total winter precipitation across southwest Asia, including the KH, according to ENSO and MJO conditions are discussed in the following section. Differences in KH precipitation between El Niño and La Niña, and similarities between phases of the MJO are in agreement with the extreme precipitation event distributions observed here (Figs. 2 & 3).

Previous research has linked significant reductions in winter precipitation over southwest Asia to phases of the MJO that enhance convection in the eastern Indian Ocean and maritime continent (Barlow et al. 2005; Hoell et al. 2012). Contrastingly, phases that diminish convection in that tropical region enhance precipitation over southwest Asia. Based on those findings, this research originally investigated MJO influence on KH precipitation with the hypothesis that phases 3 and 4 would reduce precipitation in the KH, and that phases 7 and 8 would enhance it. While composites of precipitation conditioned on each phase of the MJO did display a large-scale precipitation signal over much of southwest Asia, precipitation differences in the KH were generally weak and spatially inhomogeneous. Furthermore, it was apparent that the MJO did not have a discernible effect on the number of extreme precipitation events in the KH in any phase (Shown in Fig. 3). Interestingly, insignificant differences in KH precipitation between phases is not due to a lack of influence of the MJO, but rather appears to be attributable to competing signals between the MJO's influence on moisture availability and dynamical forcing during WD (discussed in sections 4 and 5). MJO analyses presented in the following sections focus on combined phases 3 and 4, and combined phases 7 and 8, which represent the opposite ends of this relationship.

Additionally, the added influence of ENSO during MJO activity has an interesting effect on extreme precipitation event frequency. Inactive MJO periods experience proportionally more extreme precipitation events in the KH than all active phases during El Niño, with the exception of phases 1 and 7. In contrast, all MJO active phases experience more events than non-active periods during La Niña. Given the fact the MJO was generally less active during La Niña (68% of winter days during El Nino conditions had an active MJO, compared to 60% in La Nina), it is especially interesting that a higher proportion of La Nina condition extreme events occurred when the MJO was also active (64% of La Nina extreme precipitation events occurred during MJO active periods compared to 58% of events during El Nino conditions). The observed event frequencies under the independent and combined influences of ENSO and the MJO motivate our discussion of the influence of tropical forcing on large-scale dynamics and moisture availability, and its importance to KH precipitation.

4. MJO and ENSO Influences

The relationship between WD and extreme precipitation events in the KH depends on a number of factors that are influenced by both tropical and extratropical forcing. WD are infrequent, synoptic occurrences throughout the winter season that are fundamentally related to KH precipitation by orographic processes; however, the magnitude of orographic precipitation varies as a function of the moisture content of the flow, atmospheric stability, and cross-barrier wind speed (Roe et al. 2005). Both the WD, and the state of the background atmosphere are important in determining moisture flux, and their combined influence determines the spatial distribution and intensity of precipitation in the mountains. Cannon et al. (2015) showed that extreme precipitation in the KH can be generated by either strong cross-barrier winds, related to the position or intensity of a trough, abundant moisture, which may be related to a warm, moist airmass ahead of the front, seasonal changes in temperature, or a combination of influences. Although these mechanisms are not entirely independent, each WD in this analysis exhibited varying balances of influence between these components according to the prevailing large-scale circulation. This section discusses the influence of tropical forcing at intraseasonal and interannual scales on southwest Asia climate using composites of variables related to orographic precipitation during different phases of ENSO and the MJO. The influence of these modes on individual WD at the event-scale is discussed in Section 5.

a. Vertical Structure of Geopotential Height Anomalies

Figure 4 shows the vertical structure of geopotential height anomalies related to ENSO and MJO activity using CFSR data for the months of November through April, 1979-2013. In this analysis we investigate MJO by combining phases 3 and 4, as well as a combination of phases 7 and 8. These phases were selected as the concomitant dynamical-forcing and moisture-availability responses over southwest Asia are at opposite extremes between them, while phases 1, 2, 5 and 6 are transition phases. Only significant anomalies (above the 95^{th} confidence interval, as determined by a z-test) are displayed. Significant OLR anomalies are also displayed to identify anomalous tropical convection. The composites in Fig. 4, and for all further analysis, include only dates for the respective phase during which the other mode was neutral (e.g. La Niña conditions with no MJO activity). There were 491 El Niño dates with neutral MJO, 980 La Niña dates with neutral MJO, 399 dates in MJO phases 7 and 8 with neutral ENSO, and 414 dates in MJO phases 3 and 4 with neutral ENSO. The discrepancy between non-MJO dates during El Niño and La Niña reflects both comparatively more La Niña dates in the record, and decreased MJO activity during La Niña in the period investigated.

During El Niño (La Niña) OLR anomalies over the Maritime Continent (Fig. 4; overlaid on the 500-hPa panels) are associated with diabatic cooling (heating) and a tropically forced Rossby wave response in geopotential height anomalies over continental Asia, including southwest Asia (25-40°N; 40-80°E) (Fig. 4; 850-hPa panels). Barotropic geopotential height anomalies greater than 30gpm over southwest Asia indicate a stationary anticyclone during La Niña conditions, and the weakening of the subtropical jet (Fig. 4; 200-hPa panels), while also enhancing regional stability. Both mechanisms are unfavorable for the development or intensification of WD and extreme precipitation. Contrastingly, El Niño conditions exhibit negative geopotential height anomalies below -30gpm with barotropic structure over nearly all of continental Asia. This favors large-scale ascent and also intensifies the subtropical jet, while shifting it slightly southward. In positive ENSO conditions, large-scale circulation favors precipitation across southwest Asia and the KH, and is consistent with previously documented relationships between El Niño and ample southwest Asia precipitation (Yadav et al. 2010, Hoell et al. 2012). Interestingly, MJO activity does not have a comparable relationship with total precipitation in the KH (Fig. 10),due to differences in mid-to-upper tropospheric circulation responses to spatially similar OLR anomalies across the Indian Ocean and Maritime Continent (implying similar diabatic heating changes) at intraseasonal scales.

In MJO phases 3 and 4 during ENSO neutral conditions, significant OLR anomalies below -20W m^{-2} indicate enhanced convection and diabatic heating in the eastern Indian Ocean (Fig. 4). Positive 200-hPa and negative 500-hPa geopotential height anomalies over southwest Asia indicate that the Rossby wave response to anomalous tropical forcing exhibits a baroclinic structure over the region of interest (Fig. 4). It can also be seen that the 200-hPa Rossby wave generated anticyclone is found only over southern southwest Asia, while significant barotropic negative anomalies are observed to the north. Opposing signs of geopotential height anomalies straddling the climatological position of the subtropical jet serve to intensify the storm track in MJO phases 3 and 4. Atmospheric conditions over southwest Asia favor increased stability in the region of 200-hPa subsidence; however, the intensified jet on the northern boundary of this region, at the approximate latitude of the KH (Fig. 4; top row), actually favors more precipitation on account of stronger dynamical forcing aloft and at the mountain front. These conditions, which are reversed in MJO phases 7 and 8, are explored in more detail using 500-hPa omega, wave tracks, moisture availability and precipitation distributions.

b. Vertical Velocity

Figure 5 displays 500-hPa omega for the different phases of ENSO and MJO considered previously. The figure is illustrative of the differences between vertical velocity responses over southwest Asia to MJO and ENSO tropical forcing. During MJO influence, the 200-hPa dipole in geopotential height anomalies that straddles the subtropical jet (Fig. 4) produces opposing signs of 500-hPa omega between southwest Asia and the KH (Fig. 5). Significant omega below -2.5 x 10^{-3} Pa s^{-1} is observed over southwest Asia, where the Rossby wave response induces ascent, in MJO phase 7/8 (Fig. 5; top left). Simultaneously, the weakened jet to the north of the anticyclone generates anomalous descent at the KH orographic barrier, where dynamical forcing is reduced. While large-scale ascent augments precipitation over southwest Asia, the concomitant weakening of orographic forcing in the KH is unfavorable for precipitation in the mountains. The relationship is reversed during MJO phase 3/4, which inhibits precipitation over southwest Asia through increased subsidence, but favors dynamically forced ascent and precipitation at the KH orographic barrier (Fig. 5; top right). The vertical velocity signal is more uniform between regions under ENSO conditions, with broad-scale ascent during El Niño and subsidence during La Niña (Fig. 5; bottom left and right, respectively). These differences have important ramifications with respect to WD activity and thermodynamic balance in the region.

c. Wave Tracks

Lagrangian approaches to investigating the effect of the MJO on winter storm tracks over the Northern Hemisphere (e.g. Penny et al. 2012) have been performed previously, but an analysis specific to southwest Asia has not yet been undertaken. The frequency of 500-hPa wave tracks in each phase of ENSO and the MJO, which indicates the propagation of WD over southwest Asia (Cannon et al. 2015), is shown in Figs. 6 and 7, respectively. The tracking technique employed here is that of Cannon et al. (2015), which uses the 500-hPa signature of WD in standardized geopotential height anomalies to differentiate individual disturbances (troughs) from the background flow, and to track their propagation in the Northern Hemisphere using the day-to-day spatial correlation of cyclonic features. The advantage of this particular technique is specific to WD, which propagate along relatively low latitudes, encounter highly variable topography, exhibit strong tropical influences and are spatially complex. This method is proven to accurately identify the primary atmospheric circulation pattern that produces KH precipitation events and has been used for additional analysis of regional climate (see Cannon et al. 2015 for additional details).

Figure 6 illustrates increased WD track activity over southwest Asia during ENSO warm phases relative to neutral and cool phases, when the MJO was inactive. This corresponds with an increase in the strength of the subtropical jet (Cannon et al. 2014) and barotropic negative geopotential height anomalies over the region (Fig. 4). Contrastingly, track frequency during MJO phases without ENSO influence (Fig. 7) is increased during phases in which tropical forcing favors subsidence over southwest Asia (Phases 2-4). The discussion above indicated important differences in the vertical structure of Rossby wave responses to tropical forcing from either ENSO or the MJO (Fig. 4). The baroclinic response observed during MJO activity in the eastern Indian Ocean (phases 2-4) results in enhanced track activity, likely related to the intensification of the subtropical jet to the north of the anomalous region of subsidence, while the barotropic response during the cool phase of ENSO reduces WD activity. Takashi and Shirooka (2014) similarly show increased vertically integrated eddy kinetic energy over southwest Asia during El Niño and the negative phase of the MJO, confirming the positive influence on the region's storm track observed here using a Lagrangian approach.

d. Moisture Availability

In addition to dynamical forcing by WD impinging on topography, moisture availability is essential to orographic precipitation generation (Roe et al. 2005). Despite dissimilarities in mid-level circulation and WD activity, similar reductions in precipitation over southwest Asia between MJO phases 3/4 and La Niña (Hoell et al. 2012) may be attributable to decreased moisture flux toward the region in both cases. Figure 8 shows precipitable water and vertically integrated moisture flux anomalies for MJO phases 3/4 and 7/8, and ENSO in positive and negative phases. The reduction in available moisture during MJO phases 3/4, as indicated by significant precipitable water anomalies below -2kg m^{-2} over all of southwest Asia, greatly reduces the efficiency of orographic precipitation and cloud generation for mountainous regions of southwest Asia, despite abundant track activity (Fig. 7). Interestingly though, these generalizations for southwest Asia do not hold true for the Karakoram, where extreme topography adjacent to the climatologically moist Gangetic Plain complicates the relationship between tropical forcing by the MJO and WD precipitation. It is also important to note that the spatial distribution of vertically integrated moisture flux anomalies is nearly identical between MJO 3/4 and La Niña, as well as between MJO 7/8 and El Niño. Strong anomalous flow from southwest Asia toward the region of enhanced convection over the eastern Indian Ocean is observed in the MJO 3/4 and La Niña, and opposite flow in the MJO 7/8 and El Niño.

Despite the similarities in moisture conditions amongst phases of the MJO and ENSO, the observed temperature anomalies are not consistent (Fig. 9). El Niño, which produces anomalous moisture exceeding 2kg m^{-2} over the Indian Subcontinent, exhibits significantly negative temperature anomalies over all of southwest Asia. The more than 2°C drop in average temperature during El Niño conditions is attributable to cold air protruding further south than climatologically expected on account of the significant barotropic negative geopotential height anomalies over southwest Asia. Similar moisture conditions are observed during MJO 7/8, but temperature anomalies are of the opposite sign, as significant warming is generated by warm-air advection that balances anomalous regional ascent within the baroclinic environment (Fig. 5; top left). It is also worth emphasizing that the two modes exist on very different time scales. Interannual dry or wet periods related to ENSO likely produce significant changes in temperature and moisture via land-atmosphere feedbacks over southwest Asia that are not as well established over the relatively short duration of an MJO event.

e. Contributions of Dynamical Forcing and Moisture Availability to Precipitation

During El Niño periods without MJO activity, increased available moisture and dynamical forcing (Figs. 6 & 8) greatly enhance precipitation across southwest Asia and in the KH relative to La Niña conditions, which simultaneously limit these contributions to WD-driven precipitation (Fig. 10). Similar precipitation teleconnections are documented in previous studies (e.g. Mariotti, 2007; Yadav et al. 2010; Cannon et al. 2014). However, tropical forcing related to the MJO has a more complex relationship with the KH as dynamical forcing and moisture influences that enhance precipitation are not observed in the same phases across all of southwest Asia. For example, in MJO phases 3/4 during ENSO neutral conditions, the spatial patterns of moisture flux and precipitable water anomalies are similar to La Niña; however, large-scale descent is observed over southwest Asia (Fig. 5), which remains dry, while an intensified subtropical jet to the north, at the approximate latitude of the KH, dynamically enhances ascent at the orographic barrier (Fig. 4). In the KH, orographic forcing is thus intensified and reduced available moisture does not translate to reduced precipitation relative to phases 7/8 (Fig. 10; bottom). Compared to the rest of southwest Asia, which demonstrates significant precipitation differences amongst MJO phases (Barlow et al. 2005), orographic precipitation in the KH benefits from more moisture, which is garnered from the Arabian Sea and recycled from the Gangetic Plain (Curio et al. 2015), and higher topography, which increases the effectiveness of dynamical forcing in generating precipitation.

f. Spatial and Temporal Patterns of Precipitation

Given the difficulties associated with modeling or measuring precipitation within the study area's heterogeneous topography (Lang and Barros, 2004; Bookhagen and Burbank, 2010; Norris et al. 2015a,b), this section evaluates the consistency of precipitation patterns related to the MJO and ENSO across data sets. Figure 11 demonstrates differences in precipitation between MJO phases 3/4 and 7/8 during ENSO neutral, and between El Niño and La Niña without MJO activity, for CFSR, APHRODITE (land only) and TRMM. Large-scale precipitation patterns associated with ENSO and the MJO are consistent amongst all three data sets. Precipitation over the eastern Indian Ocean is significantly enhanced in MJO 3/4 and La Niña, on account of the location of related tropical convection in the eastern Indian Ocean and Maritime Continent (note that Aphrodite does not cover oceanic areas). Additionally, all three datasets are consistent in indicating increased precipitation over southwest Asia in MJO 7/8 and El Niño. These similarities lend confidence to the robustness of the large-scale pattern of precipitation associated with the observed changes in dynamics and moisture related to tropical forcing (Fig. 10).

On a regional scale, orographic precipitation is less consistent amongst datasets. Though TRMM, APHRO and CFSR record significantly more precipitation throughout the majority, if not all, of the KH during El Niño than La Niña, large discrepancies exist between MJO phases. APHRODITE estimates significantly more precipitation in the KH during MJO 3/4, while CFSR and TRMM do not indicate a significant difference between phases. This discrepancy accentuates that the magnitude and distribution of precipitation in the KH is not consistent amongst datasets due to persistent biases in each product. The better-established differences at interannual scales (ENSO) mask this issue, while intraseasonal differences (MJO) are less defined and more prone to discrepancies. Comparisons between these precipitation dataset's climatologies have been performed previously (Palazzi et al. 2013; Cannon et al. 2014, 2015). TRMM particularly struggles with estimating solid-state precipitation at high elevations of the KH (Barros et al.

2000, 2006), and one reason for the strong bias toward increased precipitation in MJO phase 7/8 may be that increased temperatures in this phase produce proportionally more liquid precipitation at low elevations of the KH, which is better detected relative to heavy precipitation in phase 3/4. Unfortunately, APHRODITE has considerable issues in estimating precipitation in the KH that are related to the dearth of stations and their interpolation, while CFSR is too coarse to adequately resolve orographic precipitation processes and is also subject to deficiencies in model physics and parameterizations of meteorological processes. Thus, it is not possible to definitively state that any single data source is better than the others.

In order to avoid difficulties related to precipitation estimates across datasets, the emphasis of this research is on extreme precipitation events, the timing of which are more consistent amongst datasets given that the largest magnitude events are typically the most widespread and well-recorded across all platforms (Cannon et al. 2014; 2015). Thus, the relationship between tropical forcing and WD events is consistent and robust, irrespective of the precipitation dataset used, because the days for which meteorological variables are investigated are consistent. Throughout the remainder of the manuscript only mechanisms that control orographic precipitation are considered, while the magnitude and spatial distribution of precipitation is not further investigated.

5. Individual Event Dynamics

Typically, 4-6 WD contribute more than half of the total seasonal precipitation (Table 2), though the exact number varies annually (Cannon et al. 2015). Beyond the few days during which these events affect the region, the relationships between global modes of atmospheric variability and KH climate are of minor consequence for observed precipitation (though temperature and cloud cover changes, which are not discussed here, may remain important for overall hydrology). Therefore, this section is dedicated to investigating differences in dynamical forcing and moisture availability within the region's atmosphere, on account of tropical forcing, on the day of WD-related extreme precipitation. Composites of individual extreme events in each phase of MJO and ENSO activity are used to identify key differences in WD attributes that alter their relationship with orographic precipitation in the KH. As in Section 4, ENSO influences are considered for dates when the MJO was inactive and MJO activity is investigated only during ENSO neutral conditions. We observe WD to account for extreme precipitation events across all phases of MJO and ENSO (Fig. 3), though extreme precipitation is achieved by unique contributions of dynamical forcing, moisture availability, and stability to orographic forcing.

Figure 12 shows composites of 500-hPa geopotential height and precipitable water anomalies for 21 extreme precipitation events in the KH occurring in El Niño conditions without MJO activity (top left), 24 events in La Niña conditions without MJO activity (top right), 13 events in the positive phase of MJO (phase 7/8) during ENSO neutral (bottom left) and 11 events in the negative phase of MJO (phase 3/4) during ENSO neutral (bottom right) in winter seasons (Nov–Apr, 1979-2012).

a. ENSO

The signature of WD in mid-troposphere geopotential height is observed during extreme precipitation in both phases of ENSO, with deep depressions to the west of the KH. The observed trough generates cyclonic flow that is perpendicular to topography in the KH (Lang and Barros, 2004; Cannon et al. 2014). Differences in the geopotential height and precipitable water fields can be understood by superimposing average WD conditions onto the background conditions associated with positive or negative ENSO phases (Section 4). El Niño conditions, associated with barotropic negative geopotential height anomalies over central Asia (Fig. 4) and an intensification of the sub-tropical jet (Yadav et al. 2010; Cannon et al. 2014), favor deeper negative anomalies that expand over a larger area during WD events. Contrastingly, an extratropical cyclone propagating across positive anomalies generated by La Niña conditions (Fig. 4) exhibits less zonal structure and more of a shortwave pattern. Shallow anomalies (-82gpm minimum compared to -95gpm minimum in El Niño) in this case are indicative of weakened cyclonic flow and diminished dynamical forcing of precipitation over topography. Precipitation differences elicited by circulation are exacerbated by additional differences in moisture availability.

ENSO related changes in surface pressure over the Maritime Continent and eastern Indian Ocean drive anomalous wind and moisture flux. Reduced convection over the Maritime Continent during El Niño relaxes equatorial Indian Ocean westerlies and reduces offshore winds from southwest Asia (Fig. 8). Precipitable water anomalies in the western Indian Ocean are significantly positive and extend northward over southwest Asia due to the weakening of the mean northeasterly moisture flux over the Arabian Sea, which curves eastward near the equator. The combination of enhanced dynamical forcing and ample moisture over southwest Asia in El Niño conditions favors high-magnitude KH precipitation during extratropical cyclones. Moisture along the cyclone's warm front is supported by the entrainment of anomalously large quantities of precipitable water over the Arabian Sea, while stronger dynamical forcing aloft enhances the intensity of orographic forcing of the moist flow. Both dynamical forcing and moisture conditions support an enhancement of orographic precipitation during WD in El Niño conditions compared to La Niña. This is presumably the reason for the observed precipitation differences at seasonal scales over southwest Asia as well as the KH (Fig. 10) (Syed et al. 2006; Yadav et al. 2010; Dimri et al. 2012; Cannon et al. 2014). Though the 1997/98 El Nino does account for 7 of 21 events in the El Nino analysis, a composite of the remaining 14 events from El Nino conditions in other years is not appreciably different from the results shown in Fig. 12. Both the magnitude and spatial distribution of anomalies are nearly identical to that of the full set of El Nino condition events (not shown).

b. MJO

In contrast to the conditions observed during ENSO activity, phases of the MJO propagation cycle that favor the dynamical enhancement of WD simultaneously suppress available moisture over southwest Asia, and vice versa. The bottom panel of Fig. 12 shows composites of significant 500-hPa geopotential height and precipitable water anomalies during extreme precipitation events in the KH, categorized by MJO phase when ENSO was neutral. It is also important to note that each composite is comprised of only 11 and 13 events, so any single event carries considerable weight. Incipient WD in MJO 3/4 propagate in conditions that favor an intensified westerly jet upstream of the KH. Negative geopotential height anomalies at 500-hPa and below (Fig. 4) favor deeper WD troughs over southwest Asia, while available moisture is at a comparative minimum. Extreme precipitation is achieved through strong dynamical forcing at the mountain front, which efficiently extracts moisture at the orographic barrier. The average geopotential height anomaly at the WD center is lower than -100gpm during negative MJO compared to -40gpm in MJO phases 7/8, and maximum precipitable water in the KH is halved from phases 7/8 to phases 3/4. During MJO 7/8, extreme precipitation events are more strongly related to abundant moisture over the western Indian Ocean, southwest Asia, and India, which is advected to the KH by comparatively weak cyclonic flow. Negative precipitable water anomalies over southwest Asia are found only in the trough, where cold air advection exists for the duration of the event. The high temperature and moisture content of the flow impinging on topography enables heavy precipitation (Krishbaum and Smith, 2008), both at the first orographic barrier as well as at subsequent peaks in the interior of the range, in the absence of strong cross-barrier winds (e.g. Norris et al. 2015a). Extreme precipitation is generated by enormous amounts of available moisture (significant anomalies in excess of 6kg m^{-2} upstream of the KH) and reduced stability, which compensate for diminished dynamical forcing in positive phases of the MJO.

6. Conclusion

Climate in the Karakoram and western Himalaya (KH) is influenced by global modes of variability at interannual and intraseasonal scales. In this work we focus on investigating how Westerly Disturbances (WD), which are the primary source of KH precipitation, are influenced by the El Niño Southern Oscillation (ENSO) and the Madden Julian Oscillation (MJO). These modes are known to modify circulation over southwest Asia by a forced Rossby wave response to changes in convection and diabatic heating over the eastern Indian Ocean/Maritime Continent. Though it is understood that no single extreme precipitation event's occurrence can be attributed to MJO activity or ENSO conditions, it is apparent that ENSO variability at interannual scales and MJO variability at intraseasonal scales have important influences on both dynamical forcing and moisture availability within westerly disturbances (WD) and thus modify the distribution of orographic precipitation in the KH. Both ENSO and the MJO produce spatially similar patterns of OLR anomalies (a proxy for diabatic heating changes) over the Maritime Continent and eastern Indian Ocean, though tropical forcing associated with each mode uniquely influences WD activity and KH precipitation. Individual extreme precipitation events in the KH were investigated to highlight each mode's relationship with regional hydrology through the systems that dominate winter climate, which is essential to understanding the current state and future fate of High Asia's water resources.

During El Niño, atmospheric conditions that support increased precipitation over southwest Asia and the KH, including the intensification and southward displacement of the subtropical jet and abundant available moisture over southwest Asia, combine to drastically increase the frequency of observed extreme precipitation events relative to La Niña or neutral conditions. In La Niña conditions WD have minimal available moisture and exist in an environment that opposes dynamical enhancement, and thus extreme precipitation events in the KH are proportionally less frequent. The period of reduced extreme event frequency at the start of the 21st century that is defined by a strong and persistent La Niña is consistent with a well-documented catastrophic drought over southwest Asia (Argawala et al. 2001). However, it is important to note that even in the La Niña years, when large-scale dynamics inhibit the development of strong WD with abundant moisture, extreme precipitation events still occur with only one-to-two fewer events observed per season relative to the climatology. This is attributable to the influence of tropical forcing associated with the MJO, as discussed in this manuscript, and to extratropical influences on the strength and moisture content of WD, which are not discussed here.

Based on the Jones (2009) MJO index, the distribution of extreme events across phases of the MJO is relatively uniform, with the exception of phase 5, in which dynamic and thermodynamic conditions that are unfavorable for the development of orographic precipitation persist over southwest Asia. This is the transition period between moisture limited WD in phases 3/4 of the MJO and dynamical forcing limited WD in phases 7/8. A reduction of available moisture over southwest Asia similar to La Niña conditions is observed in MJO phases 3/4, but dynamical forcing of WD is intensified, as reflected by deeper troughs in event composites, likely related to intensification of the subtropical jet north of the upper-level anticyclone. The occurrence of extreme precipitation in such conditions is contingent on dynamically intense WD as prevailing moisture and stability conditions oppose extreme precipitation. In phases of MJO variability that favor enhanced available moisture over southwest Asia (phases 7/8), the intensity of WD and related cross-barrier winds in the KH are reduced. Extreme precipitation events in the mountains in phases 7/8 are largely driven by warm, moist unstable flow in absence of strong dynamical forcing. Competing contributions from dynamical and thermodynamic mechanisms exist across all phases of the MJO, and have a significant influence on the processes that produce regional extreme precipitation.

It is apparent that the MJO does not favor extreme precipitation in any one phase, but rather that the influence of dynamic and thermodynamic mechanisms that drive extreme precipitation during WD evolves as the MJO propagates. This is extremely important in understanding the influence of competing modes of variability on the relationship between WD and KH precipitation. Given the fact the MJO was generally less active during La Niña compared to El Niño, it is especially interesting that a higher proportion of this ENSO phase's extreme events occurred when the MJO was also active.. Extreme events occurring during La Niña are comparatively more dependent on the influence of the MJO to generate the necessary dynamic and thermodynamic conditions to achieve heavy orographic precipitation in the KH. This is due to the persistence of unfavorable large-scale conditions for the development and enhancement of extreme-precipitation WD in La Niña conditions. It is also noteworthy that, of 205 extreme events in the KH, 34 occurred in ENSO neutral seasons when the MJO was inactive, which emphasizes that there are influences on WD and KH precipitation beyond those related to tropical forcing. Teleconnections other than the MJO and ENSO, and extratropical forcing, are outside the scope of this paper, but remain relevant to understanding KH hydrology.

The unique relationships between global variability and KH precipitation discussed here are a consequence of the region's unique geographical setting and climate, which juxtaposes a warm ocean with the world's highest mountains, in the path of the subtropical jet. Similar relationships would not be expected in many other regions around the globe. This research has demonstrated that extreme precipitation events in the KH are related to different contributions of dynamical forcing and moisture availability within WD, according to tropical forcing at intraseasonal and interannual scales. Independent and joint variability in tropical forcing by ENSO and MJO-driven diabatic heating must become major considerations of long-term evaluations of KH hydrology. Deconstructing the relationship between regional precipitation and global modes of variability allows for the evaluation of the individual components, which may not behave consistently under future climate conditions. For example, it is essential to understand the role of moisture, independent of circulation, because in a warming climate moisture availability will change exponentially with temperature (Held and Soden, 2006; Hartmann et al. 2013). Additionally, extratropical circulation, including the position and intensity of midlatitude jets, will undergo significant changes (Fu and Lin, 2011) as 21st century warming manifests changes in global temperature gradients (Lemke et al. 2007; Hartmann et al. 2013), which the IPCC has only begun to address (Christensen et al. 2013). Consequently, hypotheses of WD behavior under ENSO or MJO influence that do not account for individual contributing components will be drastically different between current and future climate conditions. These weather-climate relationships will lead to improved forecasting of WD precipitation (Schubert et al. 2002; Barlow et al.

2005), and long-term predictability of water resources over southwest Asia and the KH (Immerzeel et al. 2009; Palazzi et al. 2013; Ridley et al. 2013; Kapnick et al. 2014).

Continued research should additionally utilize regional climate models to investigate how changes in temperature, humidity, and wind at the orographic barrier, which are related to global modes of variability, modify mesoscale spatial and temporal distributions of snowfall in the KH during WD events. The influence of dynamic and thermodynamic contributions to orographic precipitation are likely increasingly complex at these scales, and will be necessary to understand in order to evaluate regional hydrology in future climate scenarios. Continued progress toward identifying the effect of global climate on Karakoram and western Himalaya hydrology will ultimately benefit hundreds of millions of people that are dependent on the region's water resources.

Acknowledgements

This research was supported by the Climate and Large-Scale Dynamics Program, from the National Science Foundation (NSF award-AGS 1116105) and by NASA Headquarters under the NASA Earth and Space Science Fellowship Program (Grant Number 13-EARTH13F-26). The CFSR data used in this research were developed by NOAA's National Centers for Environmental Prediction (NCEP) and provided by NCAR. NCEP/NCAR R1 and NOAA OLR data was provided by the NOAA/OAR/ESRL PSD, Boulder, Colorado, from their website (http://www.esrl.noaa.gov/psd/). APHRODITE data were provided by the Environment Research & Technology Development Fund of the Ministry of the Environment, Japan. TRMM data were provided by an international joint project sponsored by the Japan National Space Development Agency (NASDA) and the U.S. National Aeronautics and Space Administration (NASA) Office of Earth Science. Station data was provided by the Water and Power Development Authority of Pakistan (WAPDA) and the Pakistan Meteorological Department (PMD). The authors would also like to thank Dr. Elisa Palazzi and Dr. Mathew Barlow for their help on this manuscript.

References

Anders AM, Roe GH, Hallet B, Montgomerey DR, Finnegan NJ, Putkonen J (2006) Spatial patterns of precipitation and topography in the Himalaya. Geol Soc Am Spec Pap 398:39-53

Archer DR, Fowler HJ (2004) Spatial and temporal variations in precipitation in the Upper Indus Basin, global teleconnections and hydrological implications. Hydrol Earth Syst Sc 8:47-61

Argawala S, Barlow M, Cullen H (2001) The drought and humanitarian crisis in central and southwest Asia: A climate perspective. IRI Special Report 01-11,24pp

Barlow M, Wheeler M, Lyon B, Cullen H (2005) Modulation of daily precipitation over southwest Asia by the Madden-Julian oscillation. Mon Weather Rev 133:3579-3594

Barnston AG, Livezey RE (1987) Classification, seasonality and persistence of low-frequency atmospheric circulation patterns. Mon Wea Rev 115:1083-1126

Barros AP, Joshi M, Putkonen J, Burbank DW (2000) A study of the 1999 monsoon rainfall in a mountainous region in central Nepal using TRMM products and rain gauge observations. Geophys Res Lett 27:3683-3686

Barros AP, Chiao S, Lang TJ, Burbank D, Putkonen J (2006) From weather to climate – Seasonal and interannual variability of storms and implications for erosion processes in the Himalaya. Geol Soc Am Spec Pap 398:17-38

Bolch T, Kulkarni A, Kaab A, Huggel C, Paul F, Cogley JG, Frey H, Kargel JS, Fujita K, Scheel M, Bajracharya S, Stoffel M (2012) The state and fate of Himalayan glaciers. Science 336:310-314

Bookhagen B, Burbank DW (2006) Topography, relief and TRMM-derived rainfall variations along the Himlaya. Geophys Res Lett 33:L08405

Bookhagen B, Burbank DW (2010) Towards a complete Himalayan hydrological budget: The spatiotemporal distribution of snow melt and rainfall and their impact on river discharge. J Geophys Res-Earth 115

Cannon F, Carvalho LMV, Jones C, Bookhagen B (2014) Multi-annual variations in winter westerly disturbance activity affecting the Himalaya. Clim Dyn 44:441-455

Cannon F, Carvalho LMV, Jones C, Norris J (2015) Winter westerly disturbance dynamics and precipitation in the western Himalaya and Karakoram: a wave-tracking approach. Theor Appl Climatol doi:10.1007/s00704-015-1489-8

Christensen JH, Krishna Kumar K, Aldrian E, An SI, Cavalcanti IFA, de Castro M, Dong W, Goswami P, Hall A, Kanyanga JK, Kitoh A, Kossin J, Lau NC, Renwick J, Stephenson DB, Xie SP, Zhou T (2013) Climate Phenomena and their Relevance for Future Regional Climate Change. In: Climate Change 2013: The Physical Science Basis. Contribution of Working Group I to the Fifth Assessment Report of the Intergovernmental Panel on Climate Change [Stocker, T.F., D. Qin, G.-K. Plattner, M. Tignor, S.K. Allen, J. Boschung, A. Nauels, Y. Xia, V. Bex and P.M. Midgley (eds.)]. Cambridge University Press, Cambridge, United Kingdom and New York, NY, USA.

Curio J, Maussion F, Scherer D (2014) A twelve-year high-resolution climatology of atmospheric water transport on the Tibetan Plateau. Earth Syst Dynam 6:109-124

Dimri AP, Dash SK (2012) Wintertime climatic trends in the western Himalayas. Climatic Change 111:775-800

Dimri AP, Niyogi D, Barros AP, Ridley J, Mohanty UC, Yasunari T, Sikka DR (2015) Western disturbances: a review. Rev Geophys 53:225-246

Filippi L, Palazzi E, von Hardenberg J, Provenzale A (2014) Multidecadal variations in the relationship between the NAO and winter precipitation in the Hindu-Kush Karakoram. J Clim doi:10.1175/JCLI-D-14-00286.1

Fu Q, Lin P (2011) Poleward shift of subtropical jets inferred from satellite-observed lower-stratospheric temperatures. J Clim 24:5597-5603

Gill AE (1980) Some simple solutions for heat-induced tropical circulation. Quart J Roy Meteor Soc 106:447-462

Gong DY, Wang SW, Zhu JH (2001) East Asian winter monsoon and Arctic Oscillation. Geophys Res Lett 28:2073-2076

Hartmann DL, Klein Tank AMG, Rustucci M, Alexander LV, Bronnimann S, Charabi Y, Dentener FJ, Dlugokencky EJ, Easterling DR, Kaplan A, Soden BJ, Thorne PW, Wild M, Zhai PM (2013) Observations: Atmosphere and Surface in: Climate Change 2013: The Physical Science Basis. Contribution of Working Group I to the Fifth Assessment Report of the Intergovernmental Panel on Climate Change [Stocker TF, Qin D, Plattner GK, Tignor M, Allen SK, Boschung J, Nauels A, Xia Y, Bex V, Midgley PM (eds.)] Cambridge University Press, Cambridge, United Kingdom and New York, NY, USA.

Held IM, Soden BJ (2006) Robust responses of the hydrological cycle to global warming. J Climate 19:5686-5699

Hewitt K (2005) The Karakoram anomaly? Glacier expansion and the "elevation effect", Karakoram Himalaya. Mountain Res Dev 25:332-340

Hewitt K (2014) Glaciers of the Karakoram Himalaya: Glacial environments, processes, hazards and resources. Springer, Dordrecht, Netherlands

Hoell A, Barlow M, Saini R (2012) The leading pattern of intraseasonal and interannual Indian Ocean precipitation variability and its relationship with Asian circulation during the Boreal cold season. J Climate 25:7509-7526

Hoell A, Barlow M, Saini R (2013) Intraseasonal and seasonal-to-interannual Indian Ocean convection and hemispheric teleconnections. J Clim 26:8850-8867

Hoell A, Barlow M, Wheeler MC, Funk C (2014) Disruption of El Niño-Southern Oscillation teleconnections by the Madden Julian Oscillation. Geophys Res Lett 41:998-1004

Huffman GJ et al (2007) The TRMM multisatellite precipitation analysis (TMPA): Quasi-global, multiyear, combined-sensor precipitation estimates at fine scales. J Hydrometeorol 8:38-55

Immerzeel WW, Droogers P, de Jong SM, Bierkens MFP (2009) Large-scale monitoring of snow cover and runoff simulation in Himalayan river basins using remote sensing. Remote Sens Environ 113:40-49

Jones C, Waliser DE, Lau KM, Stern W (2004) Global occurrences of extreme precipitation and the Madden-Julian Oscillation: Observations and predictability. J Climate 17:4575-4589

Jones C (2009) A homogeneous stochastic model of the Madden-Julian Oscillation. J Climate 22:3270-3288

Kapnick SB, Delworth TL, Ashfaq M, Malyshev S, Milly PCD (2014) Snowfall less sensitive to warming in Karakoram than in Himalayas due to a unique seasonal cycle. Nature Geosci 7:834-840

Kiladis GN, Dias J, Straub KH, Wheeler MC, Tulich SN, Kikuchi K, Weickmann KM, Ventrice MJ (2014) A comparison of OLR and circulation-based indices for tracking the MJO. Mon Wea Rev 142:1697-1715

Krishbaum DJ, Smith RB (2008) Temperature and moist-stability effects on midlatitude orographic precipitation. QJR Meteorol Soc 134:1183-1199

Krishnamurti TN (1961) The subtropical jet stream of winter. J Meteorol 18:172-191

Lang TJ, Barros AP (2004): Winter storms in the central Himalayas. J Meteorol Soc Jpn 82:829-844

Lee HT (2014) Climate algorithm theoretical basis document (C-ATBD): Outgoing longwave radiation (OLR) – Daily. NOAA's Climate Data Record (CDR) Program. CDRP-ATBD-0526, 46pp

Lee YY, Lim GY (2012) Dependency of the North Pacific winter storm tracks on the zonal distribution of MJO convection. J Geophys Res 117:1-12

Lemke, P, Ren J, Alley RB, Allison I, Carrasco J, Flato G, Fujii Y, Kaser G, Mote P, Thomas RH, Zhang T (2007) Observations: Changes in snow, ice and frozen ground. In Climate Change 2007: The Physical Science Basis. Contribution of Working Group 1 to the Fourth Assessment Report of the Intergovernmental Panel on Climate Change [Solomon S, Qin D, Manning M, Chen Z, Marquis M, Averyt KB, Tignor M, Miller HL (eds.)]. Cambridge University Press, Cambridge, United Kingdom and New York, NY USA.

Mariotti A (2007) How ENSO impacts precipitation in southwest central Asia. Geophys Res Lett 34:1-5

Matsuno T (1966) Quasi-geostrophic motions in the equatorial area. J Meteor Soc Japan 44:25-42

Maussion F, Scherer D, Molg T, Collier E, Curio J, Finkelnburg R (2014) Precipitation seasonality and variability over the Tibetan Plateau as resolved by the High Asia Reanalysis. J Climate 27:1910-1927

Norris J, Carvalho LMV, Jones C, Cannon F (2015) WRF simulations of two extreme snowfall events associated with contrasting extratropical cyclones over the Himalayas. J Geophys Res doi:10.1002/2014JD022592

Norris J, Carvalho LMV, Jones C, Cannon F, Bookhagen B (2015) The spatiotemporal variability of precipitation in the Himalaya: Validation of a one-year WRF model simulation. Clim Dyn (*submitted)*

Palazzi E, von Hardenberg J, Provenzale A (2013) Precipitation in the Hindu-Kush Karakoram Himalaya: Observations and future scenarios. J Geophys Res-Atmos 118:85-100

Palazzi E, Tahir AA, Cristofanelli P, Vuillermoz E, Provenzale A (2015) Climatic characterization of Baltoro Glacier (Karakoram) and northern Pakistan from in-situ stations. *Engineering Geology for Society and Territory*. Springer, Switzerland

Penny SM, Battisti DS, Roe GH (2012) Examining mechanisms of variability within the Pacific storm track: Upstream seeding and jet-core strength. J Climate 26:5242-5259

Rasmusson EM, Carpenter TH (1982) Variations in tropical sea surface temperature and wind fields associated with the southern oscillation/El Nino. Mon Wea Rev 111:517-528

Ridley J, Wiltshire A, Mathison C (2013) More frequent occurrence of westerly disturbances in Karakoram up to 2100. Sci Total Environ 468-469:S31-S35

Roe GH (2005) Orographic Precipitation. Annu Rev Earth Planet Sci 33:647-671

Saha S et al (2010) The NCEP Climate Forecast System Reanalysis. B Am Meteorol Soc 91:1015-1057

Schubert S, Dole R, Van den Dool H, Suarez M, Waliser D (2002) Proceedings from a workshop on prospects for improved forecasts of weather and short-term climate variability on subseasonal (2 week to 2 month) time scales. Vol. 23 NASA Tech. Memo. 2002-104606, 171pp

Singh P, Ramasastri KS, Kumar N (1995) Topographical influence on precipitation distribution in different ranges of western Himalayas. Nord Hydrol 26:259-284

Skamarock WC, Klemp BJ, Dudhia J, Gill DO, Barker DM, Duda MG, Huang XY, Wang W, Powers JG (2008) A description of the Advanced Research WRF Version 3. NCAR Technical Note – 4751STR

Syed FS, Giorgi F, Pal JS, King MP (2006) Effect of remote forcings on the winter precipitation of central southwest Asia part 1: observations. Theor Appl Climatol 86:147-160

Syed FS, Giorgi F, Pal JS, Keay K (2010) Regional climate model simulation of winter climate over Central-Southwest Asia, with emphasis on NAO and ENSO effects. Int J Climatol 30:220-235

Tahir AA, Chevallier P, Arnaud Y, Ahmad B (2011) Snow cover dynamics and hydrological regime of the Hunza River basin, Karakoram Range, Northern Pakistan. Hydrol Earth Syst Sci 15:2275-2290

Takahashi C, Shirooka R (2014) Storm track activity over the North Pacific associated with the Madden-Julian Oscillation under ENSO conditions during boreal winter. J Geophys Res Atmos 119:10663-10683

Trenberth KE (1997) The definition of El Niño. Bull Amer Met Soc 78:2771-2777

Wallace J, Lim GH, Blackmon M (1988) Relationship between cyclone tracks, anticyclone tracks and baroclinic waveguides. J Atmos Sci 45:439-462

Wheeler MC, Hendon HH (2004) An all-season real-time multivariate MJO index: Development of an index for monitoring and precipitation. Mon Wea Rev 132:1917-1932

Wilks DS (2006) Statistical methods in the atmospheric sciences. Elsevier, Burlington

Wu BY, Wang J (2002) Winter Arctic Oscillation, Siberian High and East Asian winter monsoon. Geophys Res Lett 29:1-4

Yadav RK, Rupa Kumar K, Rajeevan M (2009) Increasing influence of ENSO and decreasing influence of AO/NAO in the recent decades over northwest India winter precipitation. J Geophys Res-Atmos 114

Yadav RK, Yoo JH, Kucharski F, Abid MA (2010) Why is ENSO influencing northwest India winter precipitation in recent decades? J Climate 23:1979-1993

Figure Captions

Table 1 – Index of station names, latitude, longitude, elevation, collecting agency and date range for the 12 meteorological stations shown in Fig. 1.

Table 2 – Statistics of station precipitation include: Correlation between station precipitation and the all-station first principal component for winter months, alpha values (shape) of the gamma distribution for winter precipitation, the average annual precipitation, the percent of the annual precipitation that falls in winter (Nov. – Apr.), the percent of winter precipitation that is attributed to the extreme events investigated here, and the percent of the total annual precipitation that is attributed to extreme events.

Figure 1 – Locations of meteorological stations in the western Himalaya and Karakoram from which precipitation data was acquired. Grayshade shows topography. A number of major geographical features and country names and borders are also included. The inset map shows the location of the study region (black box) over color-shaded topography.

Figure 2 – Number of extreme precipitation events per winter season (Nov. – Apr.) and categorization based on ENSO conditions. Red line indicates mean number of events during 9 El Niño seasons. Blue line indicates mean for 9 La Niña seasons. Gray line indicates mean for 15 ENSO neutral seasons. Black line identifies a 7-year running mean.

Figure 3 – Percentage of extreme precipitation events in each phase of MJO activity with specified ENSO conditions (Nov-Apr, 1979-2012). The percentage is calculated by dividing the number of events in each phase by the total number of days.

Figure 4 – Composites of geopotential height anomalies at 200, 500 and 850-hPa (bottom row) for El Nino, La Nina, MJO phases 7 and 8 and MJO phases 3 and 4. Composites include all dates of a given index in its respective phase during which the other index was not active. The top row for ENSO and MJO panels include 200-hPa wind anomaly vectors, and the green line indicates the mean position of the core of the subtropical jet (> 40m/s) during Nov to Apr. The 3000m elevation contour of the Tibetan Plateau is illustrated by a thick black line in all panels. OLR anomalies (contours; negative values are dashed) are included in the 500-hPa panels to indicate the approximate location of enhanced tropical convection related

to ENSO and MJO. Only significant values are displayed. The green box in 850-hPa panels indicates southwest Asia and the pink box indicates the Karakoram.

Figure 5 – Composites of significant (z-test $p<0.05$) 500-hPa omega anomalies during MJO phases 7 and 8 (top left), MJO phases 3 and 4 (top right), El Niño (bottom left), and La Niña (bottom right). Composites include all dates of a given index in its respective phase during which the other index was not active (Nov. – Apr. 1979-2013). The 3000m-elevation contour of the Tibetan Plateau is illustrated by a thick black line. OLR anomalies (purple contours; negative values are dashed) indicate the approximate location of enhanced tropical convection related to ENSO and MJO. Only significant values are displayed.

Figure 6 – 500-hPa wave track density (number of tracks recorded divided by the number of days in the given ENSO phase when MJO was inactive) map indicating trajectories of centers of disturbances recorded during Neutral (top), El Niño (middle) and La Niña (bottom) ENSO conditions, Nov. to Apr. 1979-2013. The 3000m-elevation contour of the Tibetan Plateau is identified by a thick black line.

Figure 7 – 500-hPa wave track density (number of tracks recorded divided by the number of days in the given MJO phase when ENSO was neutral) map indicating trajectories of centers of disturbances recorded during MJO phases 1-8, Nov. to Apr. 1979-2013. The 3000m-elevation contour of the Tibetan Plateau is identified by a thick black line.

Figure 8 – Significant (z-test $p<0.05$) precipitable water and vertically integrated moisture flux anomalies for ENSO and MJO activity, as indexed in Fig. 3.

Figure 9 – Significant (z-test $p<0.05$) 2m temperature and integrated moisture flux anomalies for ENSO and MJO activity, as indexed in Fig. 3.

Figure 10 – Differences in CFSR precipitation between El Niño and La Niña (top) and MJO phases 7, 8 and 3, 4 (bottom). Values that exceed the 95th percentile confidence interval (based on a t-test) are stippled. Blue shading indicates comparatively higher precipitation accumulations in El Niño (top) and MJO 7,8 (bottom), while green shading indicates higher accumulations in La Niña (top) and MJO 3,4 (bottom).

Figure 11 – Differences in CFSR (top), APHRODITE (middle) and TRMM (bottom) precipitation between MJO phases 7, 8 and 3, 4 (left column) and between El Niño and La Niña (right column) Nov-Apr, 1998-2007. Values that exceed the 95th percentile confidence interval (based on a t-test) are stippled. Blue shading indicates comparatively higher precipitation accumulations in MJO 7, 8 or La Niña, while green shading indicates higher accumulations in MJO 3, 4 or El Niño. The red square identifies the KH.

Figure 12 – Composites of precipitable water (color) and 500-hPa geopotential height anomalies (contour; negative values are dashed) during extreme precipitation events in the Karakoram in El Niño (top left), and La Niña (top right), as well as MJO phases 7 and 8 (bottom left) and 3 and 4 (bottom right). Only events occurring when only one mode is active are shown. The red box marks the approximate location of the Karakoram. Stippling indicates significance of precipitable water anomalies above the 95th percentile confidence interval (z-test).

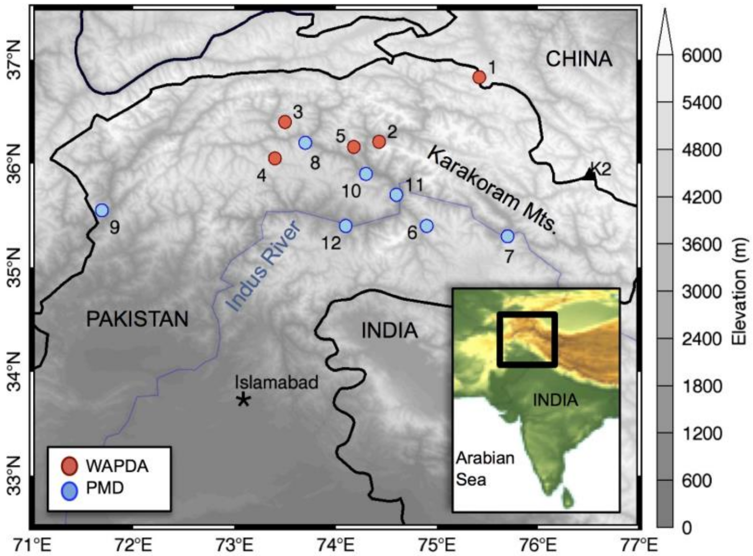

Figure 1 – Locations of meteorological stations in the western Himalaya and Karakoram from which precipitation data was acquired. Grayshade shows topography. A number of major geographical features and country names and borders are also included. The inset map shows the location of the study region (black box) over color-shaded topography.

Stations	Elev. (m)	Lat(°N)	Lon(°E)	Agency	Date Range
1. Khunjerab	4440	36.83	75.42	WAPDA	1995-2009
2. Ziarat	3020	36.21	74.43	WAPDA	1995-2009
3. Yasin	3280	36.40	73.50	WAPDA	1995-2009
4. Ushkore	3051	36.05	73.41	WAPDA	1995-2009
5. Naltar	2898	36.16	74.18	WAPDA	1995-2009
6. Astore	2168	35.33	74.90	PMD	1960-2012
7. Skardu	2317	35.30	75.68	PMD	1960-2012
8. Gupis	2156	36.16	73.40	PMD	1960-2012
9. Chitral	1498	35.85	71.83	PMD	1960-2012
10. Gilgit	1460	35.90	74.30	PMD	1960-2012
11. Bunji	1372	35.67	74.63	PMD	1960-2012
12. Chilas	1250	35.42	74.10	PMD	1960-2012

Table 1 – Index of station names, latitude, longitude, elevation, collecting agency and date range for the 12 meteorological stations shown in Fig. 1.

Stations	Correlation	Gamma (α)	Total/Year (mm)	% Wint.	% Event Wint.	% Event Tot.
Astore	0.84	0.83	477	61	60	37
Skardu	0.71	0.90	230	68	63	43
Gupis	0.55	0.79	210	46	69	31
Chitral	0.47	0.82	450	77	52	40
Gilgit	0.79	0.68	149	40	73	30
Bunji	0.83	0.93	168	40	76	31
Chilas	0.80	0.75	180	56	76	43
Average	0.71	0.81	266	64	67	36

Table 2 – Statistics of station precipitation include: Correlation between station precipitation and the all-station first principal component for winter months, alpha values (shape) of the gamma distribution for winter precipitation, the average annual precipitation, the percent of the annual precipitation that falls in winter (Nov. – Apr.), the percent of winter precipitation that is attributed to the extreme events investigated here, and the percent of the total annual precipitation that is attributed to extreme events.

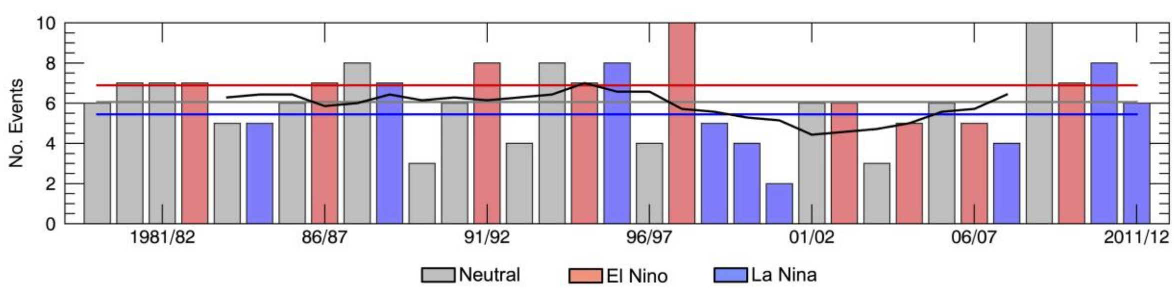

Figure 2 – Number of extreme precipitation events per winter season (Nov. – Apr.) and categorization based on ENSO conditions. Red line indicates mean number of events during 9 El Niño seasons. Blue line indicates mean for 9 La Niña seasons. Gray line indicates mean for 15 ENSO neutral seasons. Black line identifies a 7-year running mean.

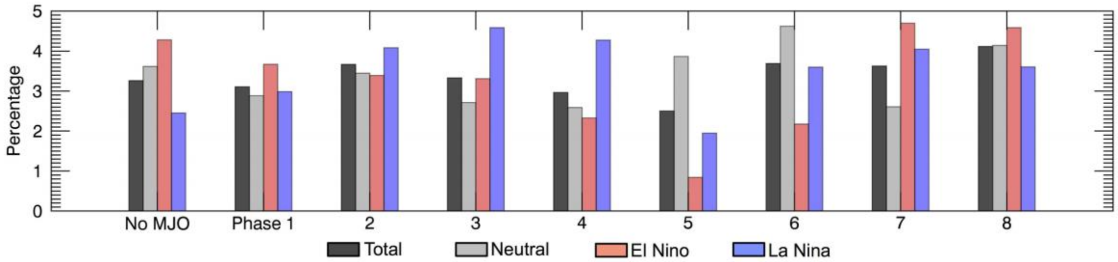

Figure 3 – Percentage of extreme precipitation events in each phase of MJO activity with specified ENSO conditions (Nov-Apr, 1979-2012). The percentage is calculated by dividing the number of events in each phase by the total number of days.

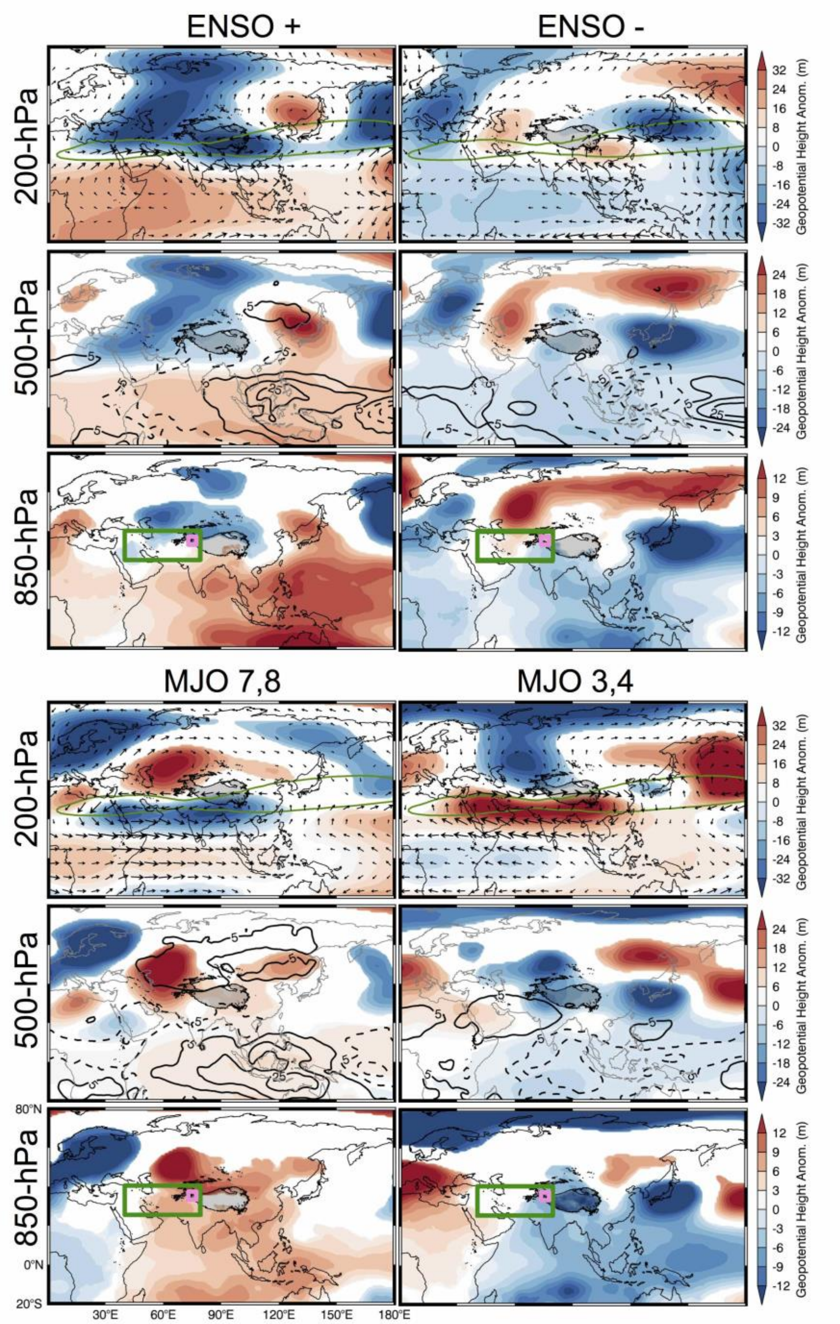

Figure 4 – Composites of geopotential height anomalies at 200, 500 and 850-hPa (bottom row) for El Nino, La Nina, MJO phases 7 and 8 and MJO phases 3 and 4. Composites include all dates of a given index in its respective phase during which the other index was not active. The top row for ENSO and MJO panels include 200-hPa wind anomaly vectors, and the green line indicates the mean position of the core of the subtropical jet (> 40m/s) during Nov to Apr. The 3000m elevation contour of the Tibetan Plateau is illustrated by a thick black line in all panels. OLR anomalies (contours; negative values are dashed) are included in the 500-hPa panels to indicate the approximate location of enhanced tropical convection related to ENSO and MJO. Only significant values are displayed (z-test p<0.05). The green box in 850-hPa panels indicates southwest Asia and the pink box indicates the Karakoram.

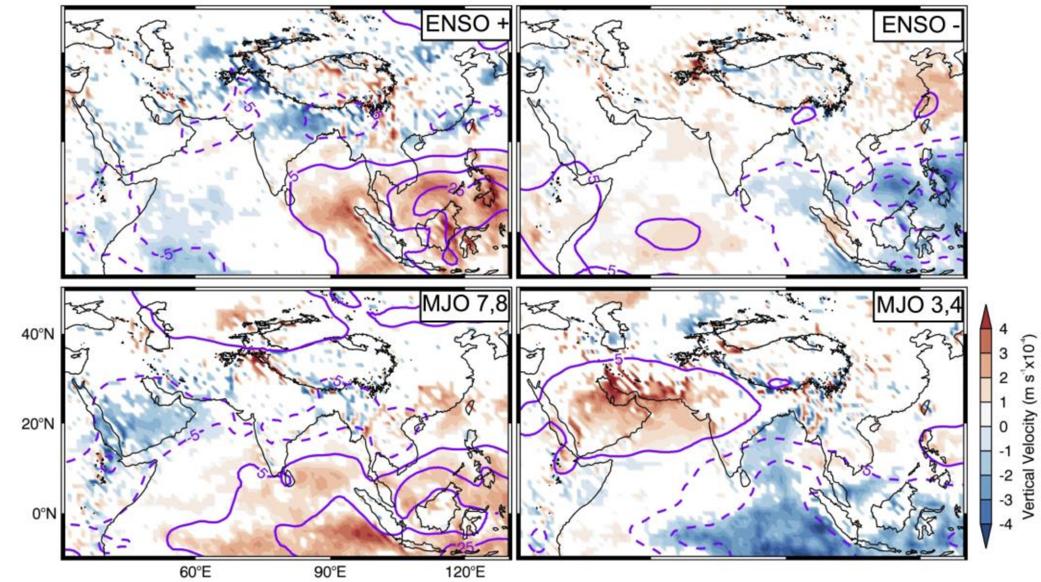

Figure 5 – Composites of significant (z-test p<.05) 500-hPa omega anomalies during MJO phases 7 and 8 (top left), MJO phases 3 and 4 (top right), El Niño (bottom left), and La Niña (bottom right). Composites include all dates of a given index in its respective phase during which the other index was not active (Nov. – Apr. 1979-2013). The 3000m-elevation contour of the Tibetan Plateau is illustrated by a thick black line. OLR anomalies (purple contours; negative values are dashed) indicate the approximate location of enhanced tropical convection related to ENSO and MJO. Only significant values are displayed.

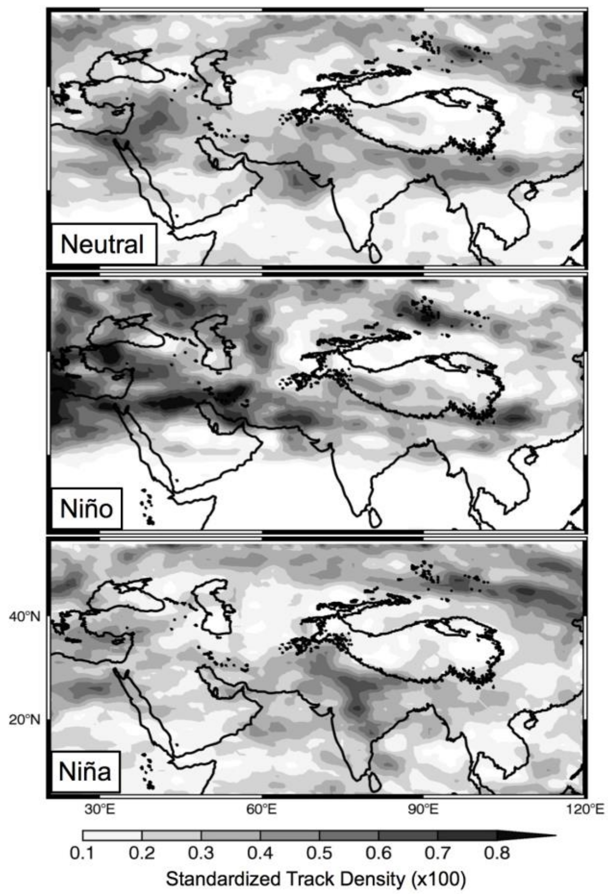

Figure 6 – 500-hPa wave track density (number of tracks recorded divided by the number of days in the given ENSO phase when MJO was inactive) map indicating trajectories of centers of disturbances recorded during Neutral (top), El Niño (middle) and La Niña (bottom) ENSO conditions, Nov. to Apr. 1979-2013. The 3000m-elevation contour of the Tibetan Plateau is identified by a thick black line.

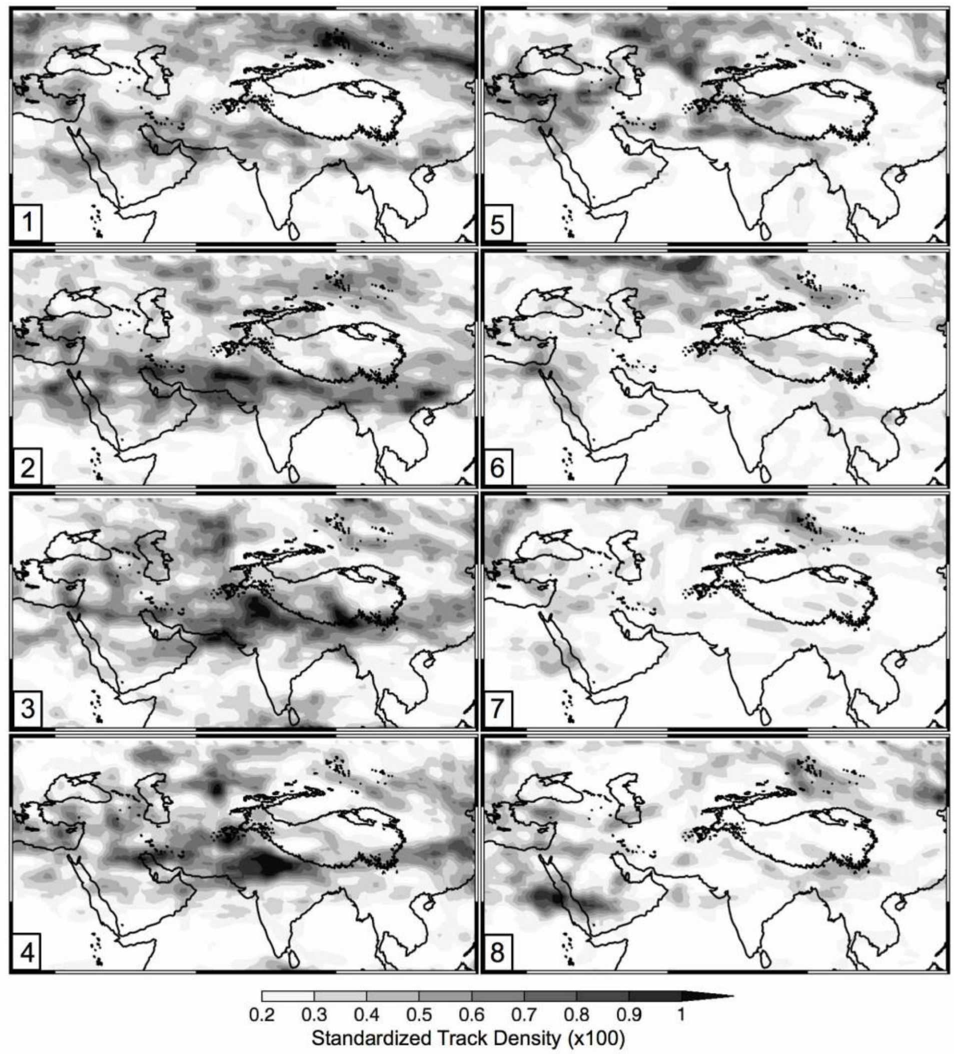

Figure 7 – 500-hPa wave track density (number of tracks recorded divided by the number of days in the given MJO phase when ENSO was neutral) map indicating trajectories of centers of disturbances recorded during MJO phases 1-8, Nov. to Apr. 1979-2013. The 3000m-elevation contour of the Tibetan Plateau is identified by a thick black line.

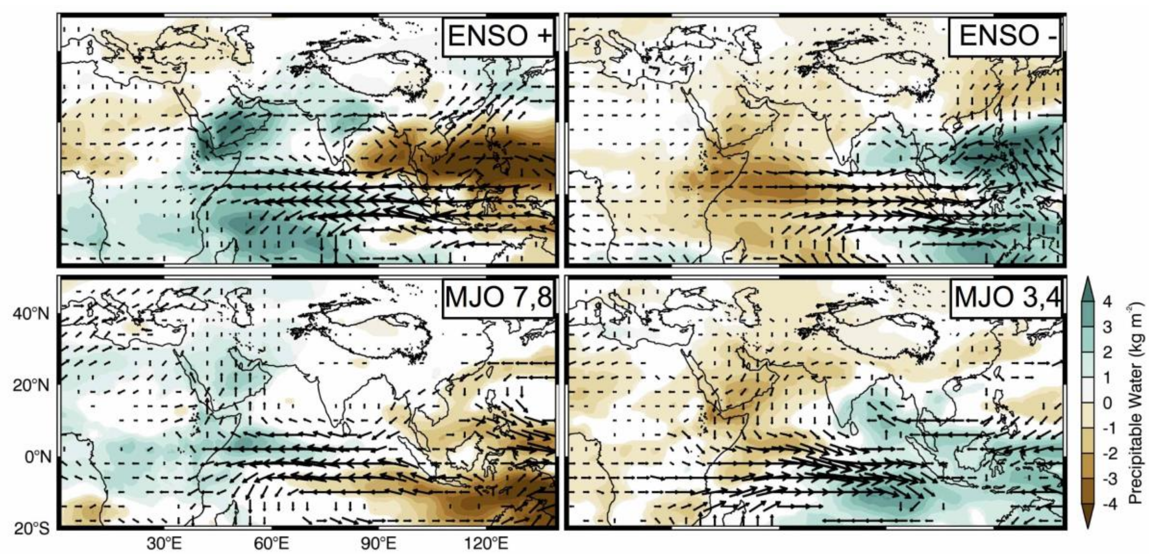

Figure 8 – Significant (z-test $p<0.05$) precipitable water and vertically integrated moisture flux anomalies for ENSO and MJO activity, as indexed in Fig. 3.

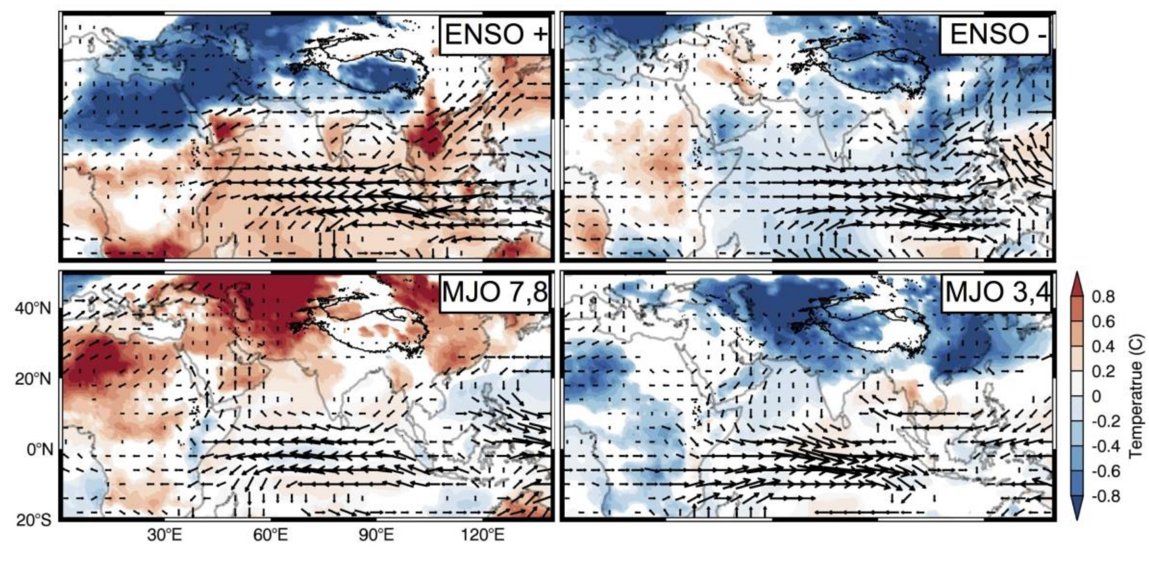

Figure 9 – Significant (z-test $p<0.05$) 2m temperature and vertically integrated moisture flux anomalies for ENSO and MJO activity, as indexed in Fig. 3.

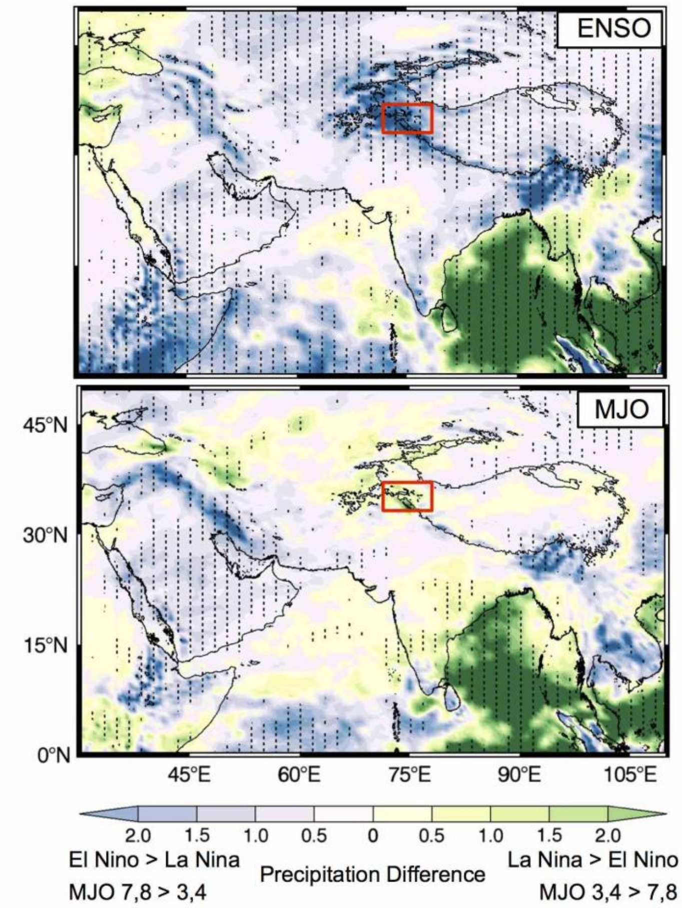

Figure 10 – Differences in CFSR precipitation between El Niño and La Niña (top) and MJO phases 7, 8 and 3, 4 (bottom). Values that exceed the 95th percentile confidence interval (based on a t-test) are stippled. Blue shading indicates comparatively higher precipitation accumulations in El Niño (top) and MJO 7,8 (bottom), while green shading indicates higher accumulations in La Niña (top) and MJO 3,4 (bottom). The red box indicates the location of the KH region.

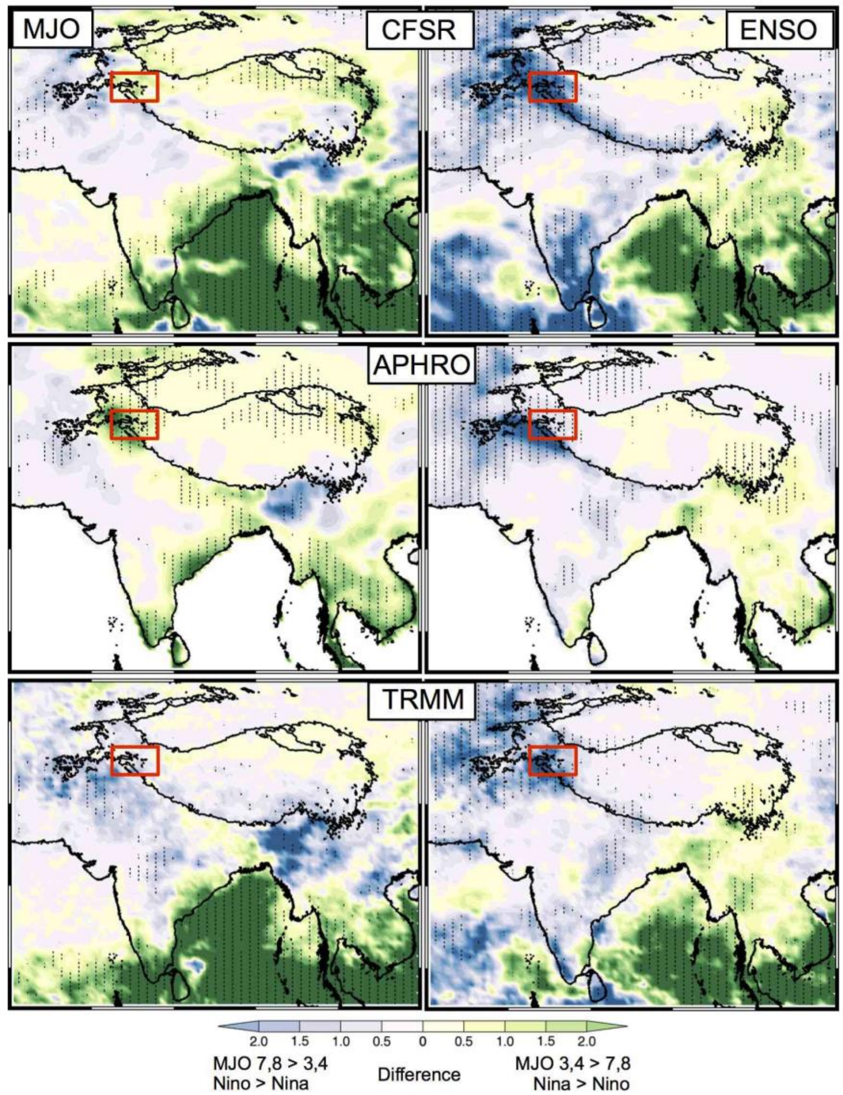

Figure 11 – Differences in CFSR (top), APHRODITE (middle) and TRMM (bottom) precipitation between MJO phases 7, 8 and 3, 4 (left column) and between El Niño and La Niña (right column) Nov-Apr, 1998-2007. Values that exceed the 95th percentile confidence interval (based on a t-test) are stippled. Blue shading indicates comparatively higher precipitation accumulations in MJO 7, 8 or La Niña, while green shading indicates higher accumulations in MJO 3, 4 or El Niño. The red square identifies the KH.

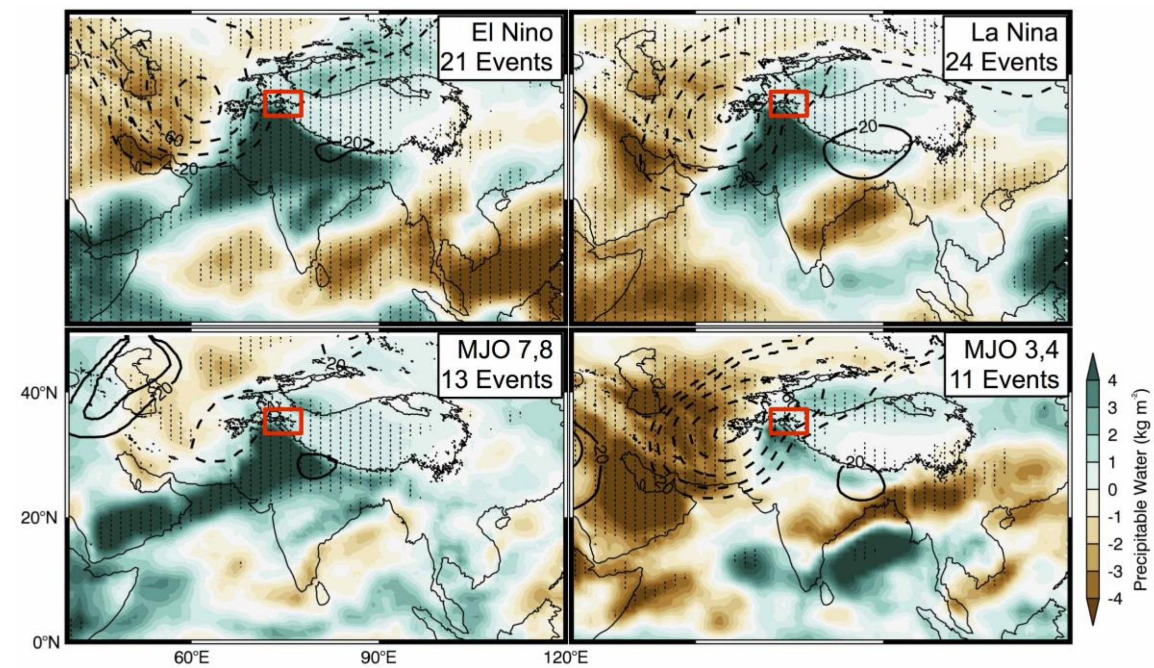

Figure 12 – Composites of precipitable water anomalies (color) and significant 500-hPa geopotential height anomalies (contour; negative values are dashed) during extreme precipitation events in the Karakoram in El Niño (top left), and La Niña (top right), as well as MJO phases 7 and 8 (bottom left) and 3 and 4 (bottom right). Only events occurring when only one mode is active are shown. The red box marks the approximate location of the Karakoram. Stippling indicates significance of precipitable water anomalies above the 95th percentile confidence interval (z-test).